Sensitivity of Squall-Line Rear Inflow to Ice Microphysics and Environmental Humidity

MING-JEN YANG* AND ROBERT A. HOUZE JR.

Department of Atmospheric Sciences, University of Washington, Seattle, Washington

(Manuscript received 9 December 1994, in final form 3 May 1995)

ABSTRACT

Two-dimensional nonhydrostatic numerical simulations of a midlatitude squall line show that the rear inflow and related aspects of storm structure are sensitive to hydrometeor types, ice-phase microphysics, and the midlevel environmental humidity. Without ice-phase microphysics, the model cannot produce realistic air motions or precipitation in the stratiform region. With the occurrence of heavy hailstones, there is no enhanced rear-to-front flow at the back edge of the storm, because of the weak midlevel mesolow in the narrow stratiform region. Evaporation is the most important latent cooling process determining the structure and strength of the descending rear inflow and the mesoscale downdraft. Latent cooling by melting snow does not initiate the mesoscale downdraft; however, it accounts for at least 25% of the strength of the maximum of rear-to-front flow at the back edge of the storm during the mature stage and enhances the strength of the mesoscale downdraft by 22%. Mesoscale downdraft is initiated above the 0°C level by sublimational cooling. With the environmental midlevel moisture reduced by half, mesoscale downdrafts are 22% stronger, but the maximum of rear-to-front flow at the back edge of the system reaches only 38% of its mature-stage intensity, as a result of a more vertically upright storm orientation, and hence the resultant weaker mesolow. These results indicate that the descending rear inflow is in part a dynamical response to the latent cooling processes in the trailing stratiform region of a squall-line-type mesoscale convective system.

1. Introduction

Squall lines with 50–200-km-wide trailing stratiform precipitation regions are an important type of organized mesoscale convective system (MCS), which occur in both the Tropics and midlatitudes (Hamilton and Archbold 1945; Newton 1950; Fujita 1955; Pedgley 1962; Zipser 1969, 1977; Houze 1977). Doppler radar observations have documented the detailed kinematic and precipitation structures of squall-type MCSs (e.g., Roux et al. 1984; Smull and Houze 1985, 1987; Biggerstaff and Houze 1991a,b, 1993). Numerical modeling has confirmed these observations (Nicholls 1987; Dudhia et al. 1987; Fovell and Ogura 1988; Rotunno et al. 1988; Weisman et al. 1988; Tao and Simpson 1989; Lafore and Moncrieff 1989; Tao et al. 1993; Skamarock et al. 1994). These studies show a mesoscale storm-relative ascending front-to-rear (FTR) flow, transporting hydrometeors rearward from a leading-edge convective line to the trailing stratiform region, and a storm-relative rear-to-front (RTF) flow, descending through the stratiform region toward low levels in the leading convective region. A conceptual model depicting these and other commonly observed features of squall-type MCSs was presented in Fig. 1 of Houze et al. (1989; see also Houze 1993, chapter 9).

Smull and Houze (1987) characterized the observed RTF flow (or rear inflow) structure of 18 mesoscale convective systems. They suggested that a midlevel mesolow in the stratiform region (Brown 1979) might act in conjunction with a mesolow in the convective region (LeMone 1983) to establish a continuous RTF current across the storm. They further suggested that in some cases (e.g., Chong et al. 1987) rear inflow could be generated by the physical processes internal to the convective system without the aid of ambient flow entering the system.

Zhang and Gao (1989) performed mesoscale model simulations of an intense midlatitude squall line indicating that the large-scale baroclinicity provided deep and favorable RTF flow within the upper half of the troposphere. The mesoscale response to convective forcing enhanced the trailing rear inflow, and latent cooling and water loading were responsible for the descent of the rear inflow.

Fovell and Ogura (1989) and Weisman (1992) showed that the RTF flow increased in strength with increasing environmental vertical wind shear and convective available potential energy (CAPE). Using a convection-resolving cloud model, Weisman (1992) further discussed how various RTF flow structures could influence the cold-pool circulation at the leading edge of the convective system, producing a stronger or weaker storm.

Corresponding author address: Ming-Jen Yang, Dept. of Atmospheric Sciences, University of Washington, Box 351640, Seattle, WA 98195-1640.
E-mail: mingjen@atmos.washington.edu

Despite these previous studies, the physical processes accounting for the structure and strength of rear inflow have not been completely identified. How sensitive is the rear inflow to hydrometeor types (especially heavy hailstones versus light snow particles)? How sensitive is the rear inflow to ice-phase microphysics? How sensitive is the rear inflow to the environmental humidity? What are the crucial microphysical processes determining the rear inflow structure? Furthermore, it has not been established whether the rear inflow is determined more by environmental factors or by physical processes internal to the storm. The objective of this study is to answer these questions.

The case investigated in this study is the 10–11 June 1985 squall line observed in the PRE-STORM project (Preliminary Regional Experiment for Stormscale Operational Research Meteorology, Cunning 1986). This storm has been extensively investigated, both observationally (Augustine and Zipser 1987; Smull and Houze 1987; Rutledge et al. 1988; Johnson and Hamilton 1988; Biggerstaff and Houze 1991a,b, 1993; Braun and Houze 1994) and numerically (Zhang et al. 1989; Zhang and Gao 1989; Tao et al. 1993; Yang and Houze 1995). However, none of these studies has completely answered the questions addressed in this study. We use a high-resolution nonhydrostatic cloud model to perform six numerical experiments in order to determine the sensitivity of the storm structure to hydrometeor types, ice-phase microphysics, and environmental humidity. Because the 10–11 June 1985 squall line has a large horizontal extent and six sensitivity test runs are required, only 2D simulations are carried out. The 2D simulation approach is justified since during the mature stage the 10–11 June squall line was highly linear and symmetric in its precipitation pattern and its cross-line airflows. A three-dimensional simulation verified that the 2D simulation is adequate for the objectives of this study (Yang and Houze 1995).

2. Model description

a. Numerical model

The numerical model used in this study [same as that in Yang and Houze (1995)] is the Klemp and Wilhelmson (1978; hereafter referred to as KW) compressible nonhydrostatic cloud model, as modified by Wilhelmson and Chen (1982). For this study, we use a 2D version. The x direction is in the direction of squall-line propagation. There is neither along-line variation nor along-line velocity. The basic-state environment is assumed constant in time and horizontally homogeneous. Large-scale motion, Coriolis force, surface drag, and radiation effects are neglected.

To increase the grid resolution in lower levels, the grid is stretched in the vertical. The vertical coordinate z is height above ground level (AGL). There are 62 grid points in the vertical. The grid size Δz of the lowest layer is 140 m; the grid size of the highest layer is 550 m; and the model top is at 21.7 km. Rigid-lid conditions are applied at the bottom and top of the domain. The horizontal grid is stretched, following Fovell and Ogura (1988). There are 455 grid points in the horizontal, and the central 315 points make up a regular fine mesh with 1-km resolution. On both sides of the fine mesh, the ratio between adjacent grid spacings is 1.075:1. The total horizontal domain size is 4814 km. The open boundary condition described by KW, with phase speed $c^* = 30$ m s^{-1}, is applied to the lateral boundaries to reduce numerical reflection. The model domain moves with the storm so that the simulated storm is always within the fine mesh. A time-splitting scheme (see KW for details) is used to provide numerical efficiency by treating sound wave (2-s time step) and cloud-scale gravity wave (6-s time step) modes separately.

b. Cloud microphysics

Microphysical bulk parameterization in the model is based on Lin et al. (1983). Five types of water condensate are included: cloud water, cloud ice, rainwater, snow, and hail. In the Lin et al. (1983) microphysical scheme, a hailstone is defined as a hail particle with a diameter of 5 mm or more, a density between 0.8 and 0.9 g cm^{-3}, and a terminal velocity between 10 and 40 m s^{-1} or more. The cloud droplets and ice crystals are assumed to be monodispersed and to have no appreciable fall speeds compared to air vertical velocity. The precipitating particles (rainwater, snow, and hail) are assumed to have exponential size distributions. Following Potter (1991), the density of water is used for snow's slope parameter λ of its size distribution function. Following Braun and Houze (1994), no density correction factor is applied to the fall speed of snow. They note that there is no experimental evidence to support the inclusion of the density correction factor for the fall speed of snow, and they found that with the density factor included one obtains unreasonably large fall speeds at upper levels.

c. Initial conditions

The smoothed initial temperature and dewpoint profiles for the simulation are from the 2331 UTC 10 June 1985 sounding of Enid (END), Oklahoma (Fig. 1a). This sounding was taken at a location in the path of the bowed part of the 10–11 June squall line (see Fig. 3 of Biggerstaff and Houze 1991a), which passed this station 4 h later. The 10–11 June squall line formed over western Kansas, where there was no sounding. The Enid sounding was far enough ahead of the squall line to be unaffected by the existing convection, yet not too far away to be completely unrepresentative of the initial environmental conditions. Extra moisture was added to the Enid sounding in low levels in order to

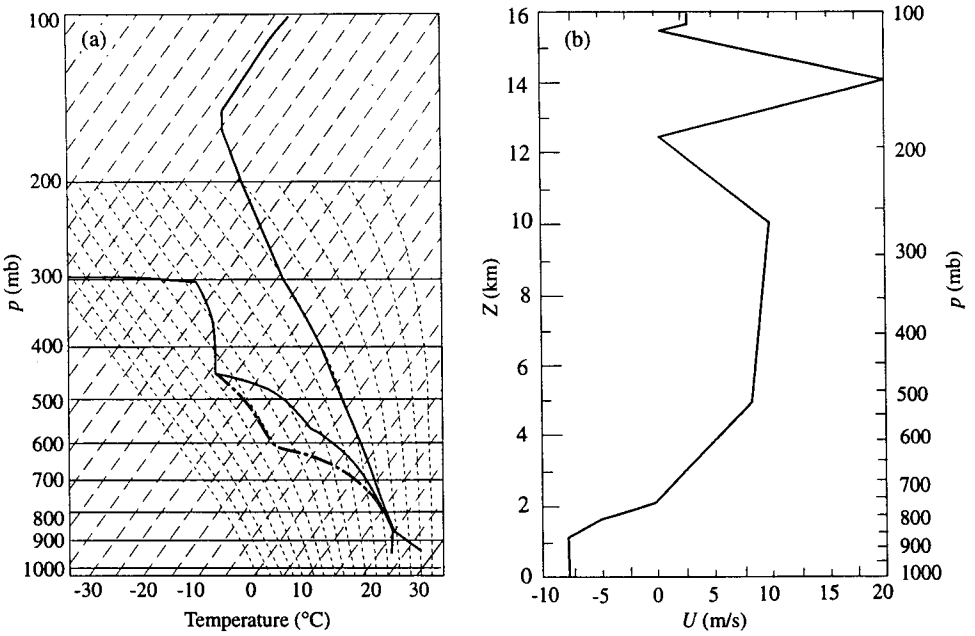

FIG. 1. (a) Temperature and dewpoint soundings displayed in a skew T–log$p$ diagram, and (b) the cross-line wind of Enid, Oklahoma, on 2331 UTC 10 June 1985 (from Yang and Houze 1995). Dash–dot line in (a) is the dewpoint profile for the DRYM run (see section 4f for details).

favor the development of convection. Without the extra low-level moisture, the simulated storm died 2 h after its initiation. The enhanced low-level moisture profile was based on the 2330 UTC 10 June 1985 sounding of Pratt, Kansas (the PTT station of Fig. 3 in Biggerstaff and Houze 1991a).

The vertical profile of the initial cross-line wind component of the Enid sounding is shown in Fig. 1b. The convective available potential energy (CAPE: Moncrieff and Miller 1976; Weisman and Klemp 1982) calculated from this sounding is 3323 J kg^{-1}, which is higher than the average value of 2820 J kg^{-1} for the springtime broken-line type of squall lines in this region (Bluestein and Jain 1985). The bulk Richardson number (Weisman and Klemp 1982; Bluestein and Jain 1985) calculated from the sounding and observed wind fields (including both the cross-line and along-line components) is 46.9, which is in the range of multicell storms (Weisman and Klemp 1982). A 5-km-deep, 170-km-long cold pool (in Fig. 2) with a 6-K potential temperature deficit ($\Delta\theta' = -6$ K) and 4 g kg^{-1} water vapor deficit ($\Delta q_v' = -4$ g kg^{-1}) was put in the domain to initiate convection. The characteristics of the cold pool were determined from the analysis of surface mesonetwork data (see Fig. 5 of Johnson and Hamilton 1988).

3. The control experiment (CNTL)

A control run (CNTL) with full model physics for 15 h has a development pattern similar to that described by Rotunno et al. (1988). Following Fovell and Ogura (1988), we turned off the hail generation processes after 6 h. Without the generation processes, hail particles were depleted within 1 h and then the only precipitating ice particle left was snow (i.e., no hail particles left after $t = 7$ h). The justification for turning off hail generation processes after the early stage is that there were very few hailstones in the mature or decaying stage of the 10–11 June squall line. Johnson and Hamilton (1988) indicated that there were some reports of

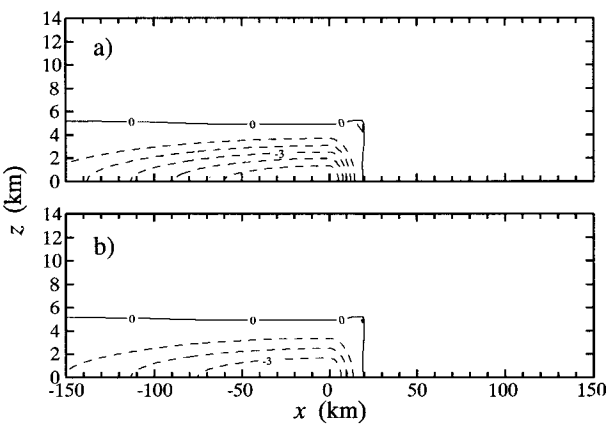

FIG. 2. (a) Potential temperature perturbation (with a contour interval of 1 K) and (b) water vapor mixing ratio perturbation (with a contour interval of 1 g kg^{-1}) of the cold pool used to initiate convection. Negative fields are dashed (from Yang and Houze 1995).

hailstones during the early stage of the 10–11 June squall line (hailfall reports from Garden City at 2210 UTC and Dodge City at 2307 UTC), but no hailfall reports were made during its mature and decaying stages (see their Fig. 7). The climatology of springtime storms in this region also indicates that hail tends to occur toward the early stages of the storms (Houze et al. 1990).

After $t = 8$ h, the simulated squall line reaches a quasi-steady state, which is realistic compared with observations. The multicellular structure has been interpreted as a gravity wave phenomenon (Yang and Houze 1995).

Objective criteria are applied to divide the simulated squall line into convective and stratiform components. A "convective region" is defined as a surface precipitation region where the rainfall rate is greater than 15 mm h^{-1}, or the gradient of rainfall rate has a magnitude greater than 5 mm h^{-1} km^{-1}. A surface precipitation region that does not satisfy the criteria above is defined as the "stratiform region." These criteria are consistent with the convective-stratiform separation method applied to radar observations by Churchill and Houze (1984).

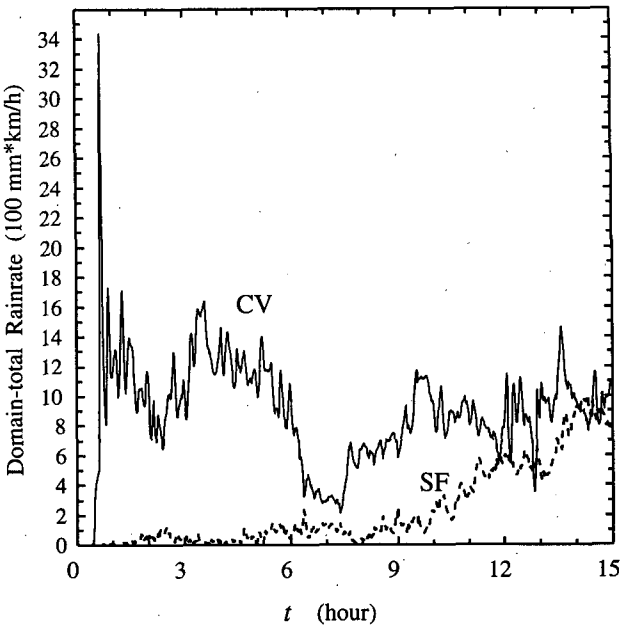

FIG. 3. Time evolution of domain total (in units of 100 mm h^{-1} km) surface convective (CV) and stratiform (SF) rainfall rates of the full-physics CNTL storm. See text for the criteria of convective and stratiform precipitation.

a. Overview of the storm development

Figure 3 shows the time series of the horizontally integrated rainfall rates over convective and stratiform regions. A substantial burst of rainfall reached the ground at $t \approx 0.5$ h in response to the initial cold pool. After the first intense rain burst, the domain-total convective rainfall became weaker and reached a somewhat steady value between 3 and 6 h. Initially ($t < 6$ h), most of the precipitation was convective. During $t = 6$–7 h, when hail generation terms were artificially turned off, convective rainfall became much weaker. After $t = 8$ h, when the simulated squall line was well developed, the convective rainfall remained roughly constant, but the stratiform rainfall increased persistently, reaching 28%–36% of total rainfall in the mature stage ($t = 10$–11 h) and 45%–53% of the total rainfall by the end of simulation ($t = 14$–15 h). The stratiform contribution (28%–36%) to total rainfall during the mature stage is in agreement with observational estimates of 29% (Johnson and Hamilton 1988) and 35%–45% (Braun and Houze 1995, unpublished manuscript).

Figures 4a–c show the surface rainfall rate over three 1-h periods (7.5–8.5 h, 10–11 h, 12.5–13.5 h) representing three stages of storm development: developing or initial (INI), mature (MAT), and slowly decaying (DEC). The simulated storm did not actually die before the end of integration (15 h), probably because of the constant convectively favorable conditions in the prestorm environment. However, after the mature stage ($t = 10$–11 h), the storm did show a slow trend of weakening or decay. During the early time (Fig. 4a), the trailing stratiform region had just begun to develop and was very narrow. During the mature stage (Fig. 4b), surface rainfall in the convective region reached its maximum intensity, and there was a broad and relatively uniform stratiform precipitation region behind the leading-edge convective line. As the system aged (Fig. 4c), the convective rainfall became less intense, and the trailing stratiform precipitation region broadened further. The evolution of surface precipitation from one stage to the next can also be seen in Fig. 4d, which shows the 1-h-averaged rainfall rates over these three periods. The secondary band of enhanced stratiform precipitation (discussed by Biggerstaff and Houze 1991a, 1993; Braun and Houze 1994) in the stratiform region shows up clearly in Fig. 4d, and it is most evident during the mature and slowly decaying stages.

To highlight the mesoscale circulations and their associated storm structures, time averaging is applied to the 2-min model output fields over the three 1-h periods. Thus transient, small-scale fluctuations are smoothed out, and only more steady mesoscale signatures are left. In Figs. 5–8, all fields are displayed in a storm-relative coordinate such that the gust front is fixed at $x = 0$ km. The cloudy region is shaded, and the storm precipitation boundary is highlighted. The cloudy region is defined as the region with a 1-h-averaged nonprecipitating hydrometeor (cloud water and cloud ice) mixing ratio greater than 0.1 g kg^{-1}. The storm precipitation boundary is defined by the contour of 1-h-averaged radar reflectivity of 15 dBZ; radar re-

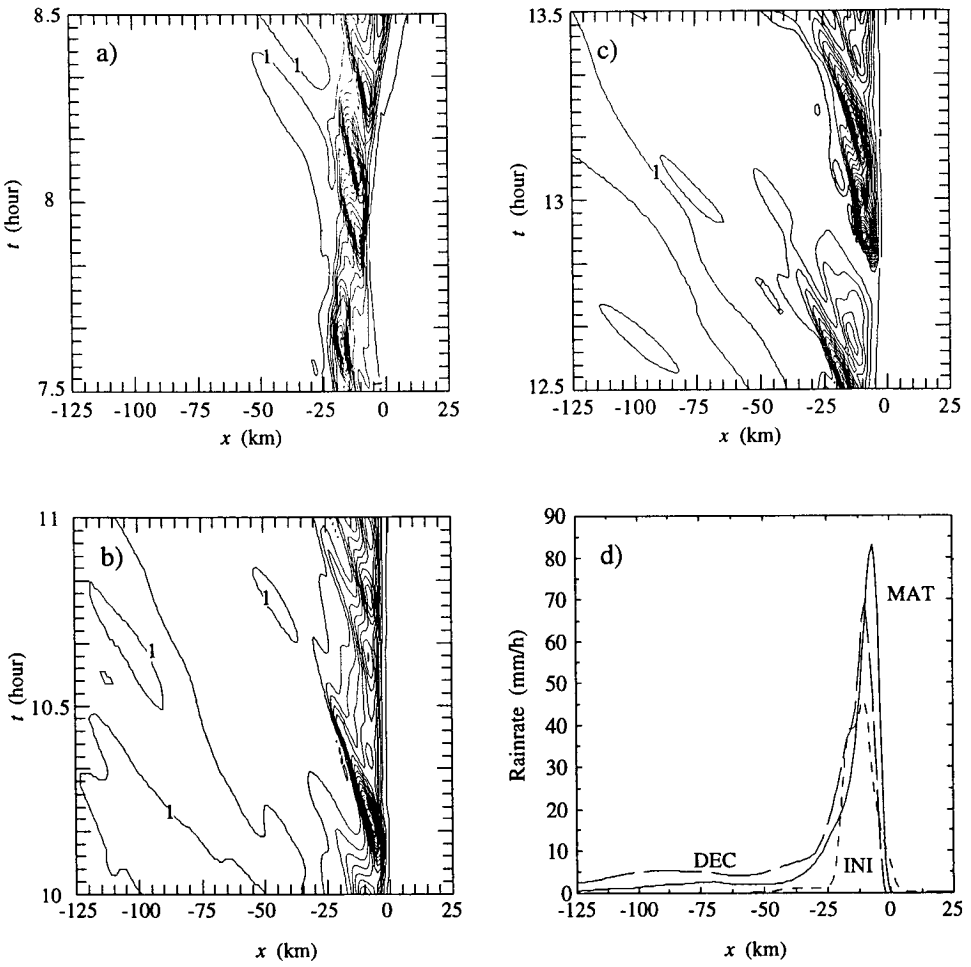

FIG. 4. Time history of surface rainfall rate during (a) the initial stage (INI; t = 7.5–8.5 h), (b) mature stage (MAT; t = 10–11 h), and (c) slowly decaying stage (DEC; t = 12.5–13.5 h) of the CNTL storm. The three 1-h-averaged surface rainfall rates of the CNTL storm are in (d). Contour lines in (a)–(c) start from 1 mm h^{-1} with an interval of 10 mm h^{-1}. These surface rainfall rate fields are displayed in a storm-relative coordinate such that the gust front is fixed at x = 0 km.

flectivity is calculated from mixing ratio fields of precipitation hydrometeors according to Eq. (1) of Fovell and Ogura (1988). Storm propagation speeds are 9.4 m s^{-1} in the initial stage (t = 7.5–8.5 h), 12.2 m s^{-1} during the mature stage (t = 10–11 h), and 12 m s^{-1} in the slowly decaying stage (t = 12.5–13.5 h). The fastest storm propagation speed is 13.8 m s^{-1} around t = 10 h, which matches the observed squall-line propagation speed of about 14 m s^{-1} (Zhang et al. 1989; Biggerstaff and Houze 1991a).

b. Evolution of the squall-line structure

Yang and Houze (1995) showed that the basic features of the full-physics CNTL run agreed well with the dual-Doppler radar analysis of Biggerstaff and Houze (1993). We now examine the evolution of the simulated squall-line structure by reference to Figs. 5–8.

1) KINEMATIC STRUCTURE

Figure 5 shows the evolution of the storm-relative horizontal wind field. Initially (Fig. 5a), there was strong inflow in the boundary layer ahead of the system, weaker and drier inflow at midlevels, and strong outflow at upper levels. A mid- to upper-level ascending FTR flow dominated inside the cloud (shaded region). Behind the cloud was a low- to midlevel descending RTF flow. Underneath the midlevel RTF flow behind the system was a low-level FTR outflow.

As the storm matured, the ascending FTR flow became stronger, broader, and more horizontally oriented (Fig. 5b). The divergence center near cloud top drifted farther rearward. The descending RTF flow became more organized with a pronounced double-core structure. One RTF maximum was at low levels within and behind the convective region. The other was near the

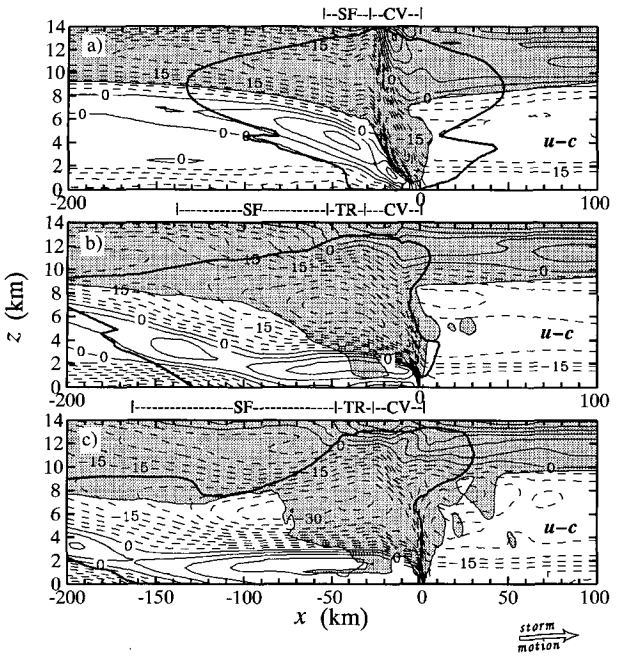

FIG. 5. Storm-relative horizontal wind ($u - c$; contour interval is 3 m s^{-1}) averaged during (a) the initial stage (t = 7.5–8.5 h), (b) mature stage (t = 10–11 h), and (c) the slowly decaying stage (t = 12.5–13.5 h) of the CNTL storm. Rear-to-front flow is in solid lines, and front-to-rear flow is dashed. Region of time-averaged nonprecipitating hydrometeor (cloud water and cloud ice) mixing ratio greater than 0.1 g kg^{-1} is shaded. Heavy outline is the storm precipitation boundary determined by the time-averaged modeled radar reflectivity of 15-dBZ contour line. Locations of convective region (CV), transition zone (TR), and stratiform region (SF) are shown in the bar above.

melting level (z = 4 km) at the back edge of the storm (x = −150 to −120 km). It developed later than the first RTF maximum, consistent with observations (Smull and Houze 1987; Rutledge et al. 1988). Lafore and Moncrieff (1989) and Weisman (1992) interpret the enhanced RTF flow at the rear of the stratiform precipitation in terms of the horizontal buoyancy gradients along the back edge of the storm that generate two counterrotating horizontal vortices, concentrating the flow from the rear of the system into the storm at midlevels (see Fig. 2c in Weisman 1992). The rear inflow plays a crucial role in supplying potentially cold and dry midlevel air from the environment to aid in the production of the convective and mesoscale downdrafts. Different orientation of the rear inflows (descending or elevated) can increase or decrease the leading-edge updraft and the storm strength, by producing different signs of additional vorticity source in the horizontal vorticity balance near the gust front (see Weisman 1992 for details).

The simulated maximum of FTR flow in the mature stage (30 m s^{-1}) is stronger than the observed one (20–25 m s^{-1}; see Fig. 3b of Biggerstaff and Houze 1993), which might be partly an effect of the enhanced horizontal mass divergence by the imposed 2D geometry (Fovell and Ogura 1988). On the other hand, the simulated maximum of RTF flow at the back edge of the storm reaches only half of the observed strength (8 m s^{-1} vs 15 m s^{-1}) during the mature stage, which might be a result of neglecting the background baroclinicity (Zhang and Gao 1989) and/or the enhanced mass convergence associated with vortices on both ends of a fully three-dimensional squall line (see Fig. 10 of Skamarock et al. 1994). By the late stage, both the FTR and RTF flows were mostly horizontally oriented (Fig. 5c).

Initially, intense convective updrafts occurred at the leading edge, dynamically induced upper-level downdrafts surrounded the intense upper-level updraft as a result of mass compensation (Houze 1993, 223–226), and precipitation-induced downdrafts were located in low levels (Fig. 6a). Mesoscale updrafts or downdrafts were not evident in the narrow stratiform region (x = −60 to −30 km) in this early stage of the storm.

There were two main updrafts in the convective region (x = −30 to 0 km in Fig. 6b) during the mature stage. At the leading edge, a low-level updraft was persistently forced by the strong convergence near the gust front. About 20 km behind the gust front, a midlevel updraft was microphysically forced by the latent warming of condensation. The transient low-level convective downdrafts are largely smoothed out by the 1-h time average.

Mesoscale ascent and descent motions were well organized in the stratiform region in the mature stage (x = −140 to −50 km in Fig. 6b). The mesoscale updraft–downdraft configuration agrees well with the along-line averaged vertical velocity field from the dual-Doppler radar composite analysis (see Fig. 3d of Biggerstaff and Houze 1993), which was taken for a portion of the storm where both the radar reflectivity and horizontal flows appeared to be the most nearly two-dimensional. In particular, the simulated mesoscale descent sloped upward toward the back of the storm, consistent with observations. Both the observations and simulation show that the mesoscale ascent motion (the broad ascent motion with $w > 0.5$ m s^{-1} at x = −130 to −50 km) was ahead of mesoscale descent motion (the broad descent motion with $w < -0.5$ m s^{-1} at x = −170 to −90 km) in the trailing stratiform region.

The level of zero vertical velocity roughly corresponded to the stratiform cloud base. The FTR–RTF flow interface (Fig. 5) had a horizontal orientation similar to that of the mesoscale updraft–downdraft interface (Fig. 6); however, it was at a slightly lower altitude than the mesoscale updraft–downdraft interface. A weak mid- to upper-level downdraft (−0.3 to −0.2 m s^{-1}) in the transition zone (x = −50 to −20 km) was located between the convective updrafts at the leading edge of the storm and the gentle mesoscale ascent in the stratiform region, although it was not shown

clearly by the contour levels. This transition-zone downdraft was also seen in the radar data (Biggerstaff and Houze 1993; Braun and Houze 1994).

Mesoscale updrafts and downdrafts were less organized and much weaker in the expanding stratiform region during the late stage (Fig. 6c). The maximum of the RTF flow at the back edge of the stratiform precipitation (Fig. 5) was collocated with the strongest mesoscale downdraft (Fig. 6), and the FTR–RTF flow interface still had an orientation similar to that of the mesoscale updraft–downdraft interface, indicating that the mass convergence associated with the ascending FTR flow and descending RTF flow in the trailing stratiform region was crucial to the generation and maintenance of mesoscale updraft and downdraft. The mid- to upper-level downdraft in the transition zone was stronger (-0.5 to -0.2 m s^{-1}) and more pronounced during the decaying stage (Fig. 6c).

2) THERMAL AND PRESSURE STRUCTURE

The potential temperature perturbation field (deviation from its initial value) in Fig. 7a shows a warm plume of air produced by latent heating in the cloudy region. Initially, adiabatic warming by the subsidence also took place over a broad region, and it propagated away from the convective region as a gravity wave bore (Mapes 1993); by t = 2 h, the gravity wave (buoyancy) bore propagates out of the fine mesh domain (not shown). A midlevel warm core was located in the stratiform region. A low-level precipitation-induced cold pool was produced by latent cooling of evaporation and enhanced by melting near the 0°C level (z = 4 km). Stretching rearward from the back edge of the cold pool head, a midlevel cold tongue ($\theta' < 1$ K) was formed by the sublimational cooling of snow particles.

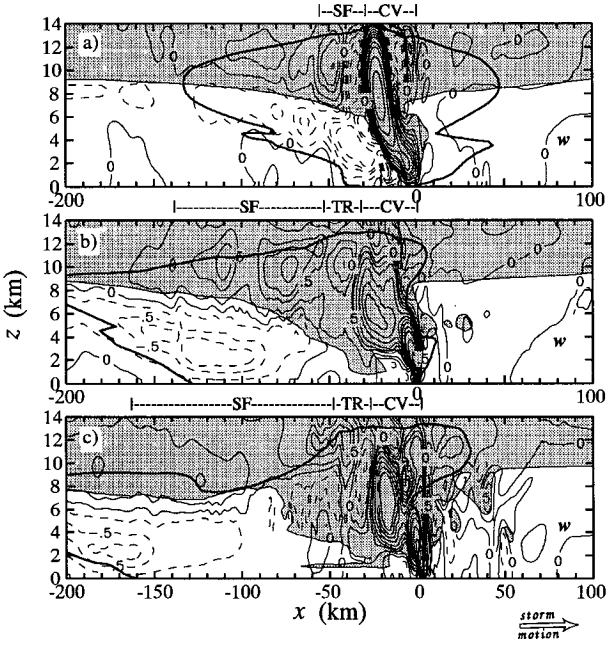

FIG. 6. Same as Fig. 5 except for the vertical velocity field w. Vertical velocity is contoured at -4, -2, -1.5, -1, -0.7, -0.5, -0.2, 0, 0.2, 0.5, 0.7, 1, 1.5, 2, 2.5, 3, 4, 5, 7, 10, and 13 m s^{-1}. Positive field is in solid lines; the negative field is dashed.

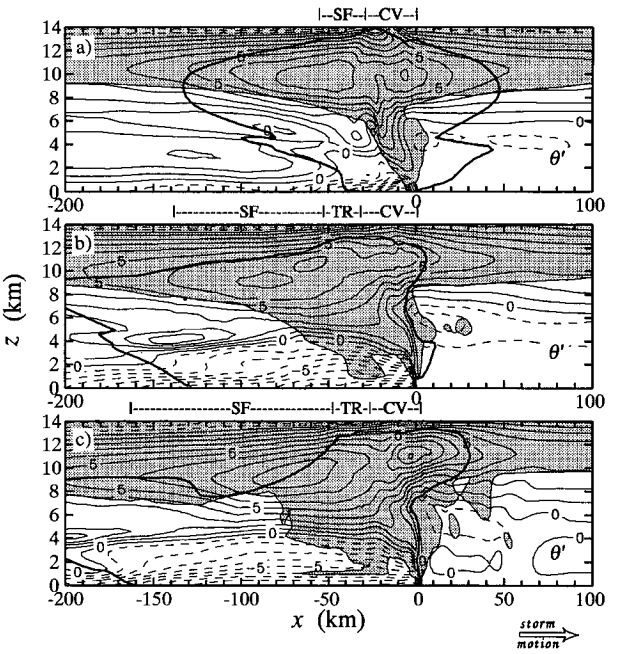

FIG. 7. Same as Fig. 5 except for potential temperature perturbation θ' (contour interval is 1 K).

As the system matured, the midlevel warm plume broadened (Fig. 7b), and the cold pool head became wider, deeper, and stronger (minimum surface θ' reached -10 K). At the back edge of the cold pool head (z = 4 to 5 km, x = -150 to -120 km), there was a local region of relatively dry and warm air, probably produced by adiabatic warming of mesoscale downdrafts as indicated by Johnson and Hamilton (1988). The midlevel warm plume broadened further (Fig. 7c) during the late stage. The cold pool head also widened; however, its strength was slightly weaker (minimum surface θ' was -9 K) in association with weaker convective activity during the slowly decaying stage.

The pressure perturbation field (deviations from initial values) in Fig. 8a shows that in the convective region there was a hydrostatically generated meso-γ-scale[1] low (LeMone 1983; Fovell and Ogura 1988; Braun and Houze 1994) just behind the convective updraft at z = 3 km. At the surface, there was a high pressure at the gust front; this gust front high pressure

[1] Meso-γ scale is defined by Orlanski (1975) as a horizontal dimension of 2–20 km.

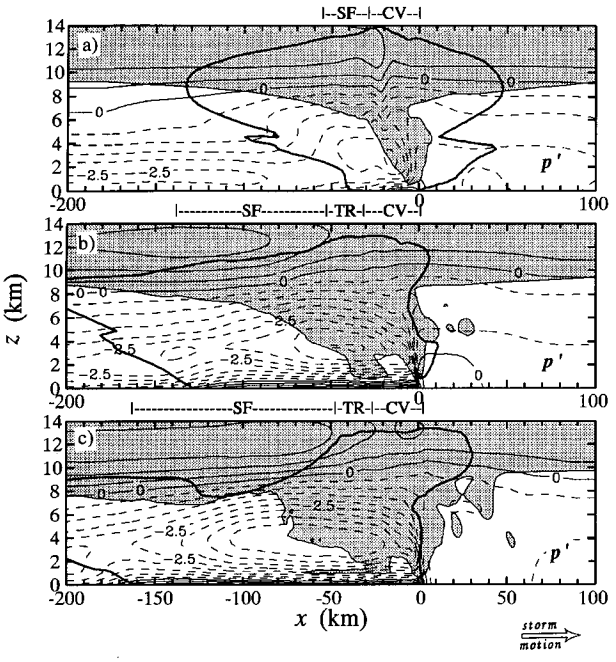

FIG. 8. Same as Fig. 5 except for pressure perturbation p' (contour interval is 0.5 mb).

was mainly dynamically generated (Fovell and Ogura 1988; Houze 1993, 364–365; Szeto and Cho 1994).

During the mature stage, the meso-γ-scale low pressure at the rear of the convective region (z = 3 to 4 km, x = 0 to 20 km in Fig. 8b) intensified as a result of increased cooling by evaporation and melting within the cold pool head. The surface gust-front high pressure reached its maximum strength (p' = 2.4 mb) when the system was well developed. In the stratiform region, the storm-induced pressure perturbation field was characterized by a broadscale pressure maximum near storm top and a pressure minimum at midlevels (z = 3 to 4 km, x = −145 to −125 km in Fig. 8b), in hydrostatic response to latent warming at upper levels and cooling at lower levels (see Fig. 7b). Braun and Houze (1994) showed a similar pressure perturbation pattern in the radar retrieval analysis of the 10–11 June storm (see their Fig. 6b). The mesolow in the stratiform region was collocated with the maximum of RTF flow at the back edge of the stratiform precipitation region (see Fig. 5b), thus supporting the argument of Smull and Houze (1987) that the resulting horizontal pressure gradient force associated with the mesolow drew midlevel air into the storm from the rear to induce the rear inflow. A weak surface wake low produced by subsidence warming of the descending rear inflow was located at the back edge of the stratiform precipitation region (x = −150 km), but it was not as evident as was observed (Johnson and Hamilton 1988). During the late stage, the meso-γ-scale low pressure in the convective region remained strong, while the gust-front high pressure weakened (Fig. 8c).

c. *Latent heating fields*

Figure 9 shows the latent heating and cooling fields averaged during the mature stage (t = 10–11 h) of the full-physics CNTL run. Figure 9a is the total latent heating field, which shows heating in the cloudy region (strongest in the convective region) and cooling in the subcloud region (strongest in the trailing stratiform region). Most of the latent heating in the cloudy region was produced by condensation of cloud water (Fig. 9b). Riming warming associated with accretion of cloud and rain droplets by snow particles occurred mostly in the convective region and also in the leading part of the stratiform region (Fig. 9c). Warming associated with depositional growth of snow occurred throughout most of the stratiform cloud region (Fig. 9d). Homogeneous freezing of cloud water into cloud ice (not shown) occurred only at upper levels and contributed very little to the total latent heating field.

Strong sublimational cooling occurred below the base of the trailing anvil cloud. This cooling is consistent with the hypothesis of Rutledge et al. (1988) that sublimational cooling of snow particles first drives the rear inflow to descend (Fig. 5b and Fig. 9d) and penetrate through the storm. Melting of falling snow particles (Fig. 9e) further enhanced the cooling near the 0°C level (z = 4 km) and strengthened (but did not initiate) the mesoscale downdrafts (details in section 4d). Most of the latent cooling in the subcloud region was produced by evaporation of rainwater (Fig. 9f). Evaporation was the most important microphysical process driving the descending rear inflow (details in section 4c).

d. *Air parcel trajectories*

Figures 10a–c show the 1-h air parcel trajectories (t = 10–11 h) calculated backward by the method of Doty and Perkey (1993) from model-generated wind fields at 2-min intervals. All trajectories are displayed in a storm-relative coordinate, in which the gust front is fixed at x = 0 km. The equivalent potential temperature θ_e along the air parcel trajectories is nearly conserved outside the convective region (x = −30 to 0 km). The maximum difference of θ_e along the trajectories is less than 2 K in the convective region.

Fifty-one air parcel trajectories ending in the broad mesoscale ascent region in the stratiform region (corresponding to $w > 0.5$ m s^{-1} at x = −130 to −50 km, z = 7 to 12 km in Fig. 6b) show that most of the air within the mesoscale ascent came from the high-θ_e boundary layer ahead of the system (Fig. 10a). Some air parcels were from the prestorm low-θ_e layer at midlevels, and a very few were from the upper levels of the transition zone.

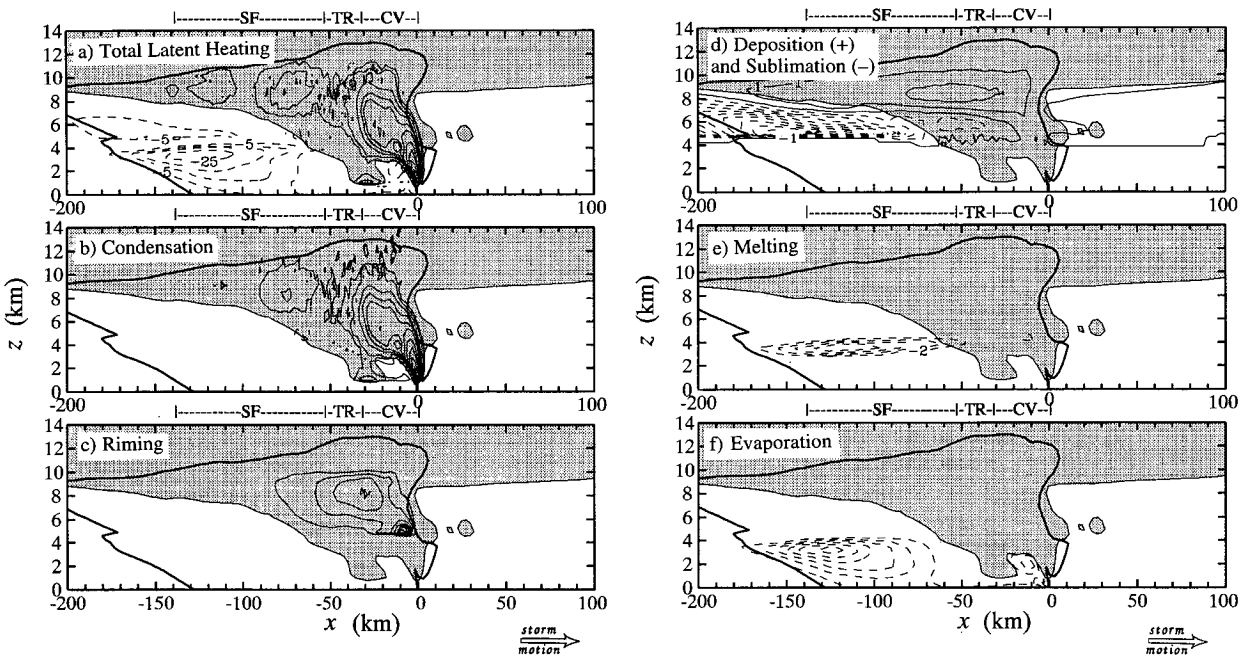

FIG. 9. One-hour-averaged mature-stage (t = 10–11 h) fields of (a) total latent heating, (b) condensational warming, (c) riming warming (contour interval is 1 K h^{-1}), (d) depositional warming and sublimational cooling (contour interval is 1 K h^{-1}), (e) melting cooling (contour interval is 2 K h^{-1}), and (f) evaporative cooling (contour interval is 4 K h^{-1}) of the CNTL storm. Latent heating in (a) and (b) is contoured at −25, −15, −10, −5, 5, 10, 20, 30, 40, 60, 100, 140, 180, and 220 K h^{-1}. The heating field is in solid lines, and the cooling field is dashed. Shaded cloudy region and the storm precipitation boundary outline are the same as in Fig. 5.

A total of 102 trajectories in the mesoscale descent region (corresponding to $w < -0.5$ m s^{-1} at $x = -170$ to -90 km, z = 1 to 6 km in Fig. 6b) determines the source of the descending air (Fig. 10b). Unlike the results of Tao and Simpson (1989), which indicated that some parts of mesoscale downdrafts originated in the rotor circulation within the cold pool head, air parcel trajectories in Figs. 10b and 10c show the mesoscale descent in the stratiform region to be distinct from the rotor circulation. Figure 10b shows that air parcels in the forward part of the mesoscale descent region were from the middle levels in the convective region and that those in the rear part of the mesoscale descent region came from the poststorm low-θ_e layer at midlevels. A 3-h (t = 9–12 h) forward trajectory analysis for air parcels in the rear inflow at the back edge of the stratiform precipitation indicates that a substantial portion of air parcels in the rear inflow descends and reaches low levels in the convective region (not shown).

Figure 10c clearly shows the rotor circulation within the head of the cold pool. Some of the air within the leading portion of the cold pool originated from the stratiform region. It entered the storm as part of the descending RTF flow from the low-θ_e layer at midlevels behind the system. Some of the air within the rotor circulation was from the low-θ_e midlevel ahead of the system, which indicates a crossover zone in the convective region (Zipser 1977; Redelsperger and Lafore 1988; Houze 1993, 363–367).

e. *Trajectories of precipitation particles*

Figure 11 displays 1-h forward-computed trajectories (t = 10–11 h) of precipitation particles starting from different vertical levels in the transition zone during the mature stage (x = 10 km in Fig. 6b). Hydrometeors are assumed to fall at their mass-weighted mean terminal velocities, which depend on time-variant amounts of hydrometeors (rain and/or snow) at each grid point. Precipitation particles falling to the surface in the transition zone were from the low levels of the convective region, while those falling to the surface in the stratiform region were from the middle to upper levels of the convective region. These findings are consistent with the results of Biggerstaff and Houze (1993) and Braun and Houze (1994).

4. Sensitivity tests

Six numerical experiments (see Table 1) are performed to determine the sensitivity of the storm structure, with emphasis on rear inflow to hydrometeor types, ice microphysics, and environmental humidity. We compare these results with those of the full-physics CNTL run. To facilitate the comparisons of these numerical experiments with the full-physics CNTL run, Fig. 12 is obtained by grouping Figs. 5b, 6b, and 7b into a separate figure to highlight the mature-stage structure of the CNTL run.

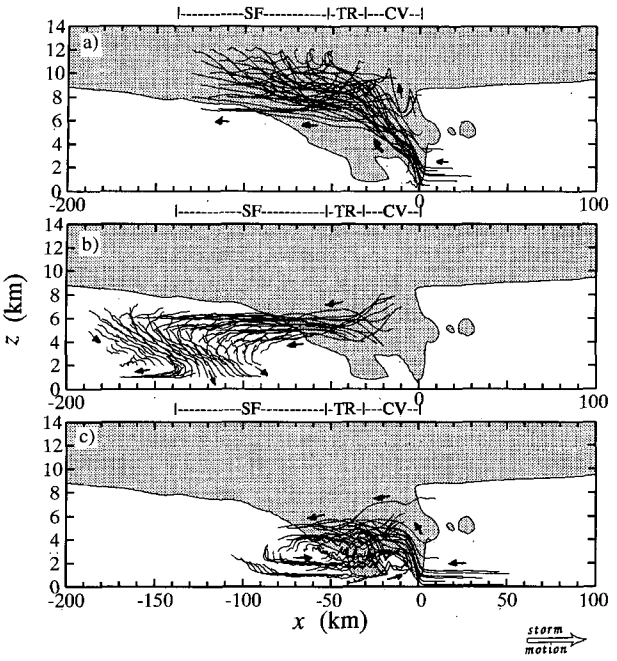

FIG. 10. One-hour (t = 10–11 h) air parcel trajectories highlight (a) the origin of mesoscale ascent, (b) the origin of mesoscale descent, and (c) the rotor circulation within the cold pool of the CNTL storm. Air parcels move in the direction of arrows. Shaded cloudy region is the same as in Fig. 5.

a. *Hailstorm simulation (HAIL)*

The experiment HAIL is the same as the CNTL run except that hail generation terms are not turned off after 6 h (i.e., allowing heavy hailstones to occur during the mature and slowly decaying stages). Owing to the large fall speeds of hail particles, hydrometeors fall out quickly, before they can be transported very far behind the convective line by FTR flows; therefore, the surface precipitation region is much narrower (60 km in Fig. 13 vs 150 km in Fig. 4d) during the mature stage (t = 10–11 h).

With the occurrence of hailstones, the multicellular structure is very pronounced in the vertical velocity field (Fig. 13b), even after the 1-h averaging. Neither the broad mesoscale updraft/downdraft nor the upper-level transition-zone downdraft occur in the HAIL storm during the mature stage. The subcloud cold pool (Fig. 13c) remains approximately the same strength (minimum surface θ' is −10 K). However, the cold pool head of the HAIL storm is much narrower (55 km wide in Fig. 13c vs 150 km wide in Fig. 12c), because the heavier hydrometeors fall out too quickly to be transported far away from the convective region. The cooling by evaporation and melting associated with these hail particles thus occurs closer to the convective region and leads to a narrower cold pool head.

The ascending FTR flow is slightly weaker and more vertically oriented (Fig. 13a). The descending RTF flow shows only one maximum—in the convective region. A second maximum of RTF flow does not occur at the back edge of the storm, as in the CNTL storm (Fig. 12a), because the horizontal pressure gradient associated with the midlevel mesolow in the stratiform region is too weak to generate an RTF wind maximum as a result of weaker buoyancy gradient at the rear of the system (Fig. 13c).

When heavy hailstones are not present during the mature stage (like the CNTL run; the only precipitating ice particles are snow particles), hydrometeors are transported farther back of the leading convective line to form a wider storm, in which mesoscale ascent and descent appear clearly (Fig. 12b). Then the thermal structure, modified by diabatic heating/cooling over a larger region, hydrostatically generates a midlevel mesolow in the trailing stratiform region to support the formation of the rear inflow. Similar results were also found in Fovell and Ogura (1988) and Tao et al. (1991). Therefore, we conclude that *the realistic structure of the simulated descending rear inflow, at least for the 10–11 June 1985 squall line, is sensitive to the assumed hydrometeor types, which affect the kinematic structure of the storm through their fallout pattern and the subsequent effects of diabatic processes on the thermal and pressure fields.*

b. *No ice-phase microphysics (NICE)*

To determine the overall effects of ice microphysics on the storm structure, we exclude the ice-phase microphysics. In this run called NICE, the simulated storm propagates more slowly (storm propagation speed is 8 m s^{-1} vs 12.2 m s^{-1}) during the mature stage (t = 10–11 h), but it has a more distinct multicellular behavior. After t = 4 h, the NICE storm reaches a "quasi-equilibrium" state (Fovell and Ogura 1988) in which convective cells are periodically generated at the leading edge with a period of 14–15 min. The mature-stage NICE storm structure (in Fig. 14) resembles the initial-stage structure of the full-physics CNTL storm (panel a of Figs. 5–8). In particular, the horizontally

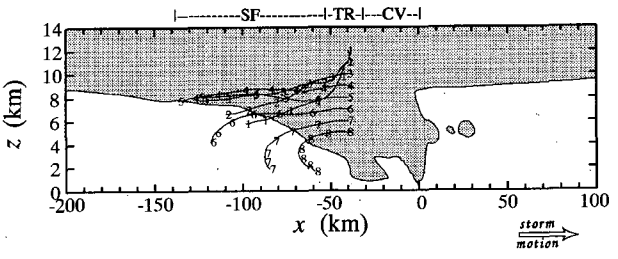

FIG. 11. One-hour (t = 10–11 h) trajectories of precipitating particles starting from different vertical levels in the transition zone for the CNTL run. Each number along the trajectories indicates the particle position every 10 min. Shaded cloudy region is the same as in Fig. 5.

TABLE 1. Design of experimental simulations.

Run	Run time	Restart time	Comments
CNTL	15 h		full physics; turn off hail generation processes after 6 h
HAIL	13 h		full physics; leave hail generation processes on after 6 h
NICE	14 h		no ice-phase microphysics
NEVP	12 h	CNTL at 3 h	no evaporative cooling
NMLT	12 h	CNTL at 3 h	no melting cooling
NSUB	12 h	CNTL at 3 h	no sublimational cooling
DRYM	12 h		drier midlevel environment; see Fig. 1a

uniform stratiform precipitation seen in CNTL during the mature and slowly decaying stages (Figs. 4b and 4c), which is mainly produced by the rearward transport, fallout, and melting of snow particles, is absent in the NICE run. Hence, the NICE storm can capture only (qualitatively) the precipitation structure within the convective region to some extent, but not the realistic stratiform precipitation region.

The vertical velocity field (Fig. 14b) displays a cellular structure, even after the 1-h time averaging. However, the mesoscale updraft/downdraft is not as broad and uniform as that in the CNTL run (Fig. 12b) and in observations (Biggerstaff and Houze 1993), and the upper-level transition-zone downdraft is absent in the NICE run. The leading-edge updraft of the NICE storm has a magnitude of 7 m s^{-1}, about 30% weaker than that (10.5 m s^{-1}) of the CNTL storm. The midlevel warm plume is much weaker (4 K in Fig. 14c vs 7 K in Fig. 12c), and the subcloud cold pool head is much narrower (60 km wide vs 150 km wide). These facts indicate that *ice microphysics have both a qualitative and quantitative impact on the storm structure, including the convective region.* The cold pool is only a little weaker (minimum surface θ' is -9 K vs -10 K); it is dominated by the evaporative cooling of rainwater in the convective region, which is still present in the NICE run.

The ascending FTR flow is somewhat weaker (-27 m s^{-1} in Fig. 14a vs -30 m s^{-1} in Fig. 12a) and more vertically oriented. The descending RTF flow shows only one maximum (located at $x = -60$ to -20 km) within a much narrower storm (surface precipitation region is 60 km wide compared to 150 km wide), although its strength is greater than in the ice-on CNTL

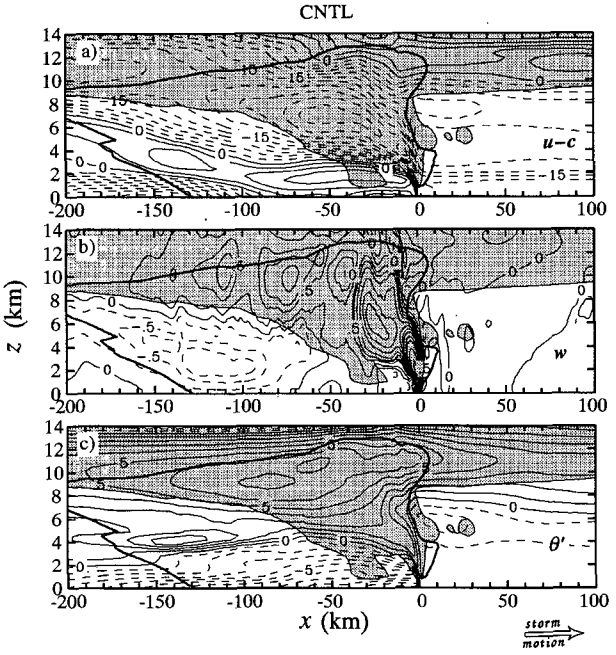

FIG. 12. (a) One-hour-averaged mature-stage (t = 10–11 h) storm-relative horizontal wind $u - c$ (contour interval is 3 m s^{-1}), (b) vertical velocity w, and (c) potential temperature perturbation θ' (contour interval is 1 K) of the CNTL storm during the mature stage. Vertical velocity in (b) is contoured at -4, -2, -1.5, -1, -0.7, -0.5, -0.2, 0, 0.2, 0.5, 0.7, 1, 1.5, 2, 2.5, 3, 4, 5, 7, 10, and 13 m s^{-1}. The positive field is in solid lines; negative field is dashed. Shaded cloudy region and the storm precipitation boundary outline are the same as in Fig. 5.

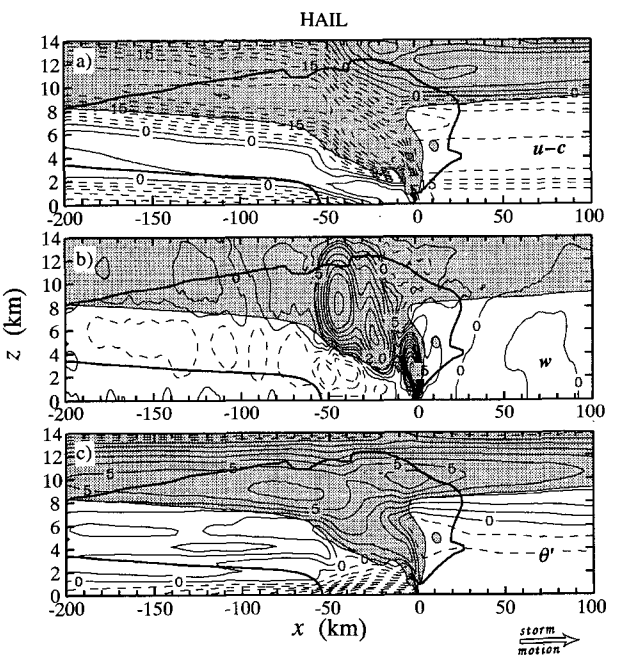

FIG. 13. Same as Fig. 12 except for the HAIL run.

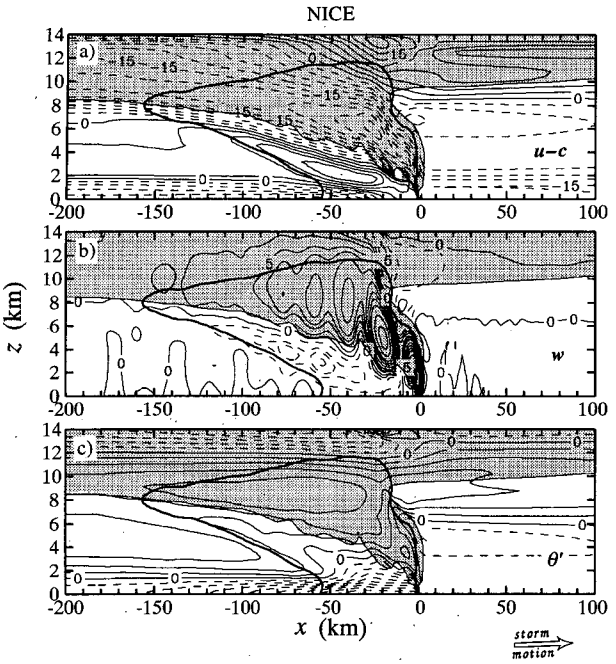

FIG. 14. Same as Fig. 12 except for the NICE run.

run (12 m s^{-1} vs 9 m s^{-1}) as indicated by Chin (1994). When ice microphysics are included (see the CNTL run in Fig. 12a), the layer of RTF flow has two maxima, one of which occurs at the back edge of the stratiform precipitation as indicated in radar analysis (Biggerstaff and Houze 1993). However, this feature is absent in the NICE run. Therefore, we conclude that *ice-phase microphysics are essential to the realistic structure of the descending RTF flow.*

c. *No evaporative cooling (NEVP)*

The experiment NEVP is the same as the CNTL run except that air is not cooled when raindrops evaporate (latent cooling by evaporation is set to zero). To speed up the simulation, the NEVP run restarts from the history file of the CNTL storm saved at $t = 3$ h. Without the latent cooling of evaporation, the NEVP storm moves very slowly, about 4–8 m s^{-1} slower than the CNTL storm. During the time period $t = 10$–11 h, the NEVP storm moves at a speed of 5 m s^{-1} versus 12 m s^{-1} of the CNTL storm.

This simulation is completely unrealistic. The results are thus quite different from that of the CNTL storm. The storm never develops an upshear tilt. As discussed in Zhang and Gao (1989), the persistently upright to downshear-tilted orientation of the NEVP storm indicates the significant effects of evaporative cooling. Without the evaporative cooling, there is no subcloud cool pool (Fig. 15c), and the system fails to show a substantial upshear tilt during the time period $t = 10$–11 h as in the CNTL run. This behavior is consistent with the theory of Rotunno et al. (1988) that the vorticity generation by the cold pool is required to overcome the vorticity associated with the environmental low-level wind shear in order for the storm to become tilted upshear.

Because of the upright to downshear-tilted system orientation, the stratiform precipitation does not trail behind the convective region but rather occurs ahead of the convective region. There is no mesoscale ascent or descent (Fig. 15b). Owing to the lack of upshear tilt of the convection, there is no midlevel mesolow behind the convective region (Fig. 19a); as a result, the mid- to upper-level FTR flow transporting hydrometeors rearward is absent (Fig. 15a). The RTF flow is elevated and entirely a consequence of strong midlevel winds in the large-scale environment overtaking and entering the storm. This NEVP sensitivity test thus supports the argument of Smull and Houze (1987) that *the descending rear inflow develops in response to dynamical and microphysical feedbacks in the trailing stratiform region.* With no trailing stratiform region, the rear inflow in the NEVP storm does not descend and penetrate through the storm but remains elevated across the system.

d. *No latent cooling by melting (NMLT)*

The experiment NMLT is the same as the CNTL run except that air is not cooled when ice particles melt (latent cooling by melting is set to zero). Like the NEVP run, the NMLT simulation restarts from the his-

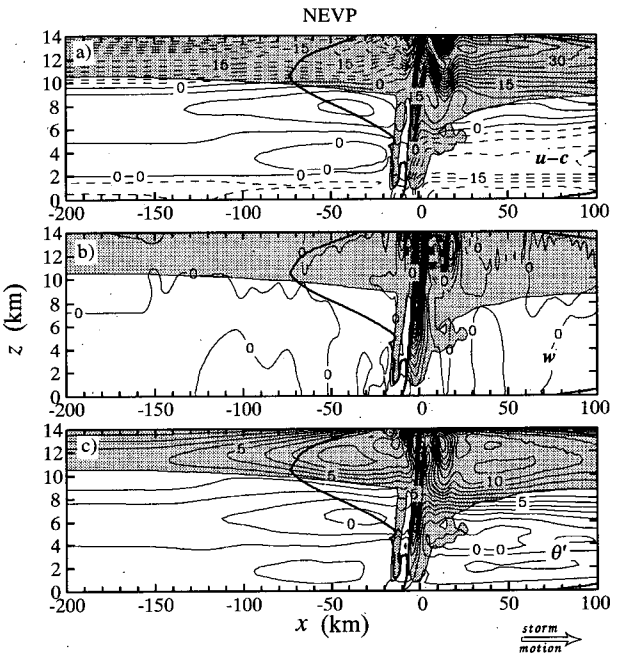

FIG. 15. Same as Fig. 12 except for the NEVP run. Vertical velocity in (b) is contoured every 2 m s^{-1}.

tory file of the CNTL run saved at $t = 3$ h. The NMLT storm generally propagates at a speed 1–2 m s^{-1} slower than the CNTL storm; however, the speed difference becomes smaller once the system becomes well developed (speed difference is only 0.2 m s^{-1} during the time period $t = 10$–11 h). The evolution of the NMLT storm is similar to the CNTL storm, although the NMLT storm reaches its mature stage slightly (0.5–1 h) later than the CNTL storm. Figure 16 shows the 1-h-average storm structure during the mature stage ($t = 10$–11 h). Although the melting cooling is turned off everywhere in the NMLT run, its simulation result is very similar to the result where melting cooling is turned off only in the stratiform region (not shown), since the dominant melting cooling process occurs in the trailing stratiform region (Fig. 9e).

Without the latent cooling by melting, the FTR flow (Fig. 16a) is much weaker (−24 m s^{-1} vs −30 m s^{-1}) and more vertically oriented. The double-core structure of the RTF flow is well preserved in the NMLT run; however, its strength is less than in the CNTL run. This result demonstrates that cooling by melting is not the cause of the rear inflow; however, the weaker rear-edge maximum of RTF flow in the NMLT run (6 m s^{-1} in Fig. 16a vs 8 m s^{-1} in Fig. 12a) indicates that *the latent cooling by melting accounts for at least 25% of the intensity of the local maximum of RTF flow at the rear of the storm during the mature stage.* The effect of melting on the stratiform region RTF flow was suggested by Smull and Houze (1987) and Rutledge et al. (1988) but it has not been demonstrated *quantitatively* before.

The updrafts at the leading edge of the NMLT storm are more upright (Fig. 16b) than in CNTL (Fig. 12b). The mid- to upper-level updrafts in the convective region are stronger, but the low-level updrafts near the gust front nose are weaker. Tao et al. (1995) obtained similar results. The maximum of the 1-h mean mesoscale ascent in the trailing stratiform region of the NMLT storm is somewhat stronger (1.3 m s^{-1} vs 1.1 m s^{-1}), but the mesoscale ascent occurs in a narrower zone (area covered by updrafts greater than 0.5 m s^{-1} is 30 km wide vs 60 km wide). Without the latent cooling by melting, the mesoscale downward motion in the trailing stratiform region is 22% weaker (−0.7 m s^{-1} vs −0.9 m s^{-1}) and 33% narrower (area covered by downdrafts less than −0.5 m s^{-1} is 40 km wide vs 60 km wide). This NMLT sensitivity test clearly shows that *cooling due to melting does not initiate the mesoscale downdrafts in the model storm, as suggested by Leary and Houze (1979); however, the melting significantly enhances the mesoscale downdrafts.* Corresponding to weaker mesoscale descent, the region of subsidence warming at the back edge of the NMLT storm (near $x = -95$ km in Fig. 16c) is 33% narrower (the packet of subsidence-warmed air defined by the $\theta' = 3$ K contour line near $z = 4$ km is 40 km wide vs 60 km wide).

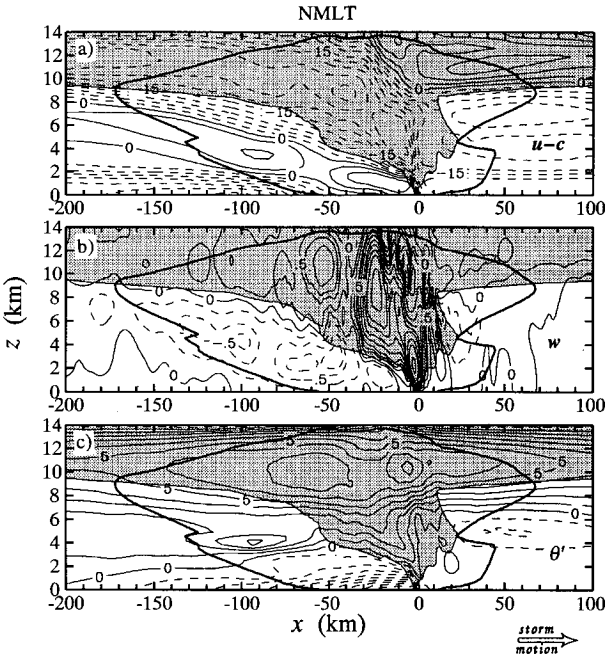

FIG. 16. Same as Fig. 12 except for the NMLT run.

e. *No latent cooling by sublimation (NSUB)*

For the NSUB experiment, air is not cooled in the process of sublimation (warming by deposition is still active). Other conditions are the same as in the CNTL run. Like the NEVP experiment, the NSUB simulation restarts from the history file of the CNTL run saved at $t = 3$ h. The evolution of the NSUB storm is similar to the CNTL run. The NSUB storm propagates at a speed 1–1.5 m s^{-1} slower than the CNTL storm, and the speed difference is 1.4 m s^{-1} during the mature stage ($t = 10$–11 h). Figure 17 displays the 1-h-average storm structure in the mature stage. Similar to the NMLT run, the simulation result of NSUB (where sublimational cooling is turned off everywhere) is almost the same as the result where sublimational cooling is turned off only in the stratiform region (not shown), since the dominant sublimational cooling process occurs in the stratiform region (Fig. 9d).

Without the latent cooling by sublimation, the ascending FTR flow (Fig. 17a) is much weaker (−24 m s^{-1} vs −30 m s^{-1}), but the maximum of descending RTF flow at the rear of the storm is only slightly weaker. Since sublimational cooling only slightly affects the strength of the enhanced rear inflow at the back edge of the system (7 m s^{-1} in Fig. 17a vs 8 m s^{-1} in Fig. 12a), we conclude that *the latent cooling by evaporation and melting are the most important microphysical processes determining the structure and strength of rear inflow in the cloud-model simulations.*

However, the observed rear inflow (Fig. 3b of Biggerstaff and Houze 1993) has stronger magnitude

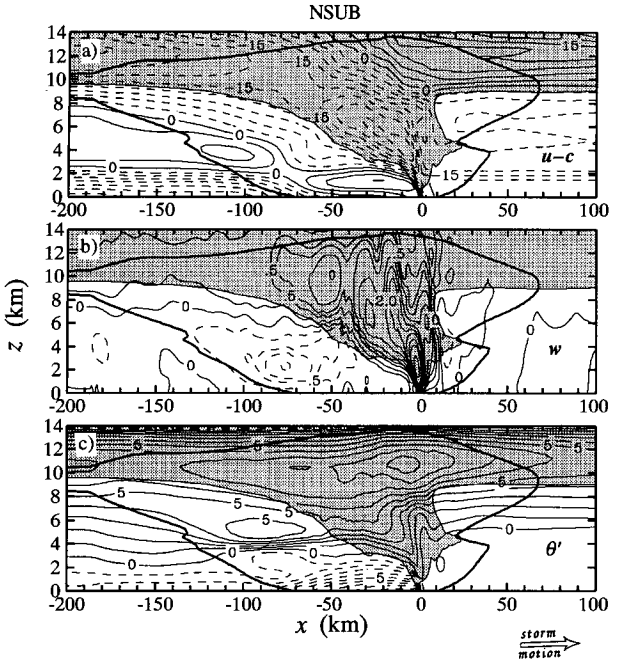

FIG. 17. Same as Fig. 12 except for the NSUB run.

(>10 m s^{-1}) and is located about 1 km above the melting level (z = 4 km). It is associated with ambient RTF flow induced by a shortwave trough in the upper troposphere (Zhang and Gao 1989). This ambient RTF flow cannot develop in the cloud model. When large-scale baroclinic processes are included (e.g., in a mesoscale model), the large-scale contribution to rear inflow can develop and occurs above the melting level; under these circumstances, the structure and strength of the rear inflow above the 0°C level is found to be more sensitive to latent cooling by sublimation (Braun 1995). The condensational heating within the ascending FTR flow and sublimational cooling at the back edge of the storm contribute to a strengthening of the large-scale trough and hence to the upper portion of the rear inflow.

The vertical velocity field of the NSUB storm (Fig. 17b) shows that the mesoscale updrafts/downdrafts in the stratiform region are much narrower (area of updraft/downdraft with magnitude greater than 0.5 m s^{-1} is 50 km wide vs 80 km wide). In particular, without the diabatic cooling by sublimation, the mesoscale downdraft (the broad downdraft less than −0.5 m s^{-1}) is initiated below the 0°C level (z = 4 km), instead of above the 0°C level as in the CNTL run (Fig. 12b) and in the observations (see Fig. 3d of Biggerstaff and Houze 1993). The comparison of model runs NSUB and CNTL thus strongly support the speculation of Rutledge et al. (1988) that *sublimational cooling at the base of the trailing anvil cloud is key to the initiation of downward air motion above the 0°C level (z = 4 km) at the rear of the storm.* Adiabatic warming associated with the mesoscale downdraft (Fig. 17c) at the rear edge of the NSUB storm is stronger (maximum θ' anomaly is 5 K vs 4 K) and occurs at a higher altitude (5 km vs 4 km), inducing a stronger mesolow at the back of the stratiform region (−3.3 mb vs −3.0 mb; not shown).

f. Drier midlevel environment (DRYM)

The experiment DRYM is the same as the CNTL run except that the initial environmental moisture at midlevels (z = 2.5–6 km or p = 800–450 mb) is reduced by approximately half (see Fig. 1a). The DRYM storm generally evolves in the same way as the CNTL storm; it initially propagates slightly faster than the CNTL storm; after t = 5 h, it propagates slightly slower. Averaged over the total integration time (12 h), the difference of the propagation speeds between the two storms is less than 1 m s^{-1}. Figure 18 shows the DRYM storm structure during the mature stage.

The DRYM storm moves at approximately the same speed as the CNTL storm during the mature stage (12.2 m s^{-1}), as a result of similar strength and depth of the cold pool (Fig. 18c). The DRYM storm is more upright and has a slightly weaker ascending FTR flow (−27 m s^{-1} in Fig. 18a vs −30 m s^{-1} in Fig. 12a). The descending RTF flow is much weaker with some FTR flow in between the two maxima of RTF flow (in the region x = −100 to −80 km). In particular, the maximum of RTF flow at the back edge of the storm has only 38% of the strength in the CNTL storm (3 m s^{-1}

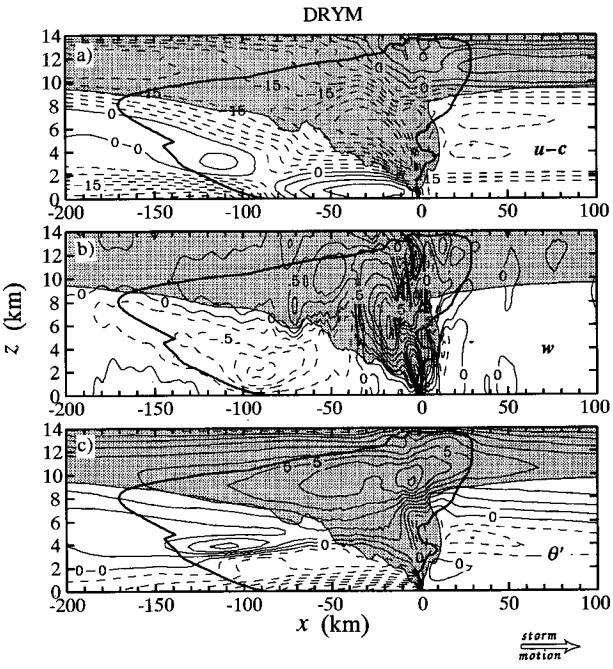

FIG. 18. Same as Fig. 12 except for the DRYM run.

vs 8 m s^{-1}). This result is counterintuitive; we expected the reduced midlevel environmental moisture to enhance the sublimational and evaporative cooling at the back edge of the system and thus to increase the local buoyancy gradients and the rear inflow strength. However, the horizontal buoyancy gradients of the DRYM storm in the stratiform region (Fig. 18c) are weaker than those of the CNTL storm (Fig. 12c).

This counterintuitive behavior is related to the more upright system orientation in DRYM compared to CNTL. The drier environmental air entrained into the leading convective region enhances evaporative cooling at midlevels (see the $\theta' < -2$ K packet at $z = 4$ to 6 km, $x = 0$ km in Fig. 18c), which counteracts the vorticity tendency produced by the cold pool (Rotunno et al. 1988; Weisman 1992) and tilts the convection into a more upright orientation. The FTR flow is reduced, and the stratiform region is narrower and weaker in most respects. With less sublimation, melting, and evaporation in the trailing portion of the stratiform region, the horizontal buoyancy gradients in the stratiform region are weaker, and the RTF flow of the DRYM storm is much weaker than that of the CNTL storm.

The vertical velocity field of the DRYM storm (Fig. 18b) shows that in the convective region, the low-level updrafts near the gust front are weaker but midlevel ones are stronger. In the stratiform region, the mesoscale downdrafts are 22% stronger (-1.1 m s^{-1} vs -0.9 m s^{-1}), as a result of an enhanced evaporative cooling associated with lower midlevel environmental humidity. In contrast, the mesoscale updrafts are weaker (0.8 m s^{-1} vs 1.1 m s^{-1}) and narrower (area enclosed by the 0.5 m s^{-1} contour is 45 km wide vs 80 km wide).

5. Role of mesolows in the formation of the descending rear-to-front flow

Smull and Houze (1987) suggested that the midlevel mesolow in the stratiform region might act in conjunction with the mesolow in the convective region to establish a broad RTF current across the storm. They further suggested that the RTF flow in some cases could be generated by "the physical processes internal to the mesoscale convective system" without the aid of ambient flow entering the system.

Zhang and Gao (1989) performed mesoscale model (MM4) simulations of the 10–11 June storm and examined the mesolow mechanism proposed by Smull and Houze (1987). In their experiment NEV, which had no resolvable-scale ($\Delta x = 25$ km in their fine mesh) evaporation and sublimation, they found that the RTF flow was weak and did not extend down to the surface, despite the occurrence of a strong midlevel mesolow (see their Fig. 13). The strong midlevel mesolow was produced by the Fritsch–Chappell (1980) convective parameterization scheme and was located in the leading convective region. This result seemed to suggest that "the midlevel mesolow mechanism proposed by Smull and Houze (1987) cannot be used alone to explain the generation of the descending rear inflow."

We investigate this question further. The Klemp–Wilhelmson cloud model used in this study constitutes a more explicit physical framework to investigate "the physical processes internal to the mesoscale convective system" referred to by Smull and Houze (1987). The model is nonhydrostatic, the convection is explicitly resolved ($\Delta x = 1$ km in our fine mesh), and the environment is horizontally uniform, so that there are no large-scale baroclinic processes active in the simulation.

The two midlevel mesolows in a squall line with a trailing stratiform precipitation region and the physical processes producing them are the phenomena that are key to understanding the ability of a mesoscale convective system to develop its own rear inflow. To investigate the role of mesolows in the formation of the descending rear inflow, we present Figs. 19 and 20, which show the storm-induced pressure perturbations with shaded RTF flow ($u - c > 5$ m s^{-1}) for three experimental simulations during the mature ($t = 10$–11 h; Fig. 19) and late stage ($t = 12.5$–13.5 h; Fig. 20). The detailed horizontal wind structures of these simulations are shown in Figs. 5b,c, 14a, and 15a.

In the no-evaporative-cooling run (NEVP; Fig. 19a), where the mesolows in both the convective and

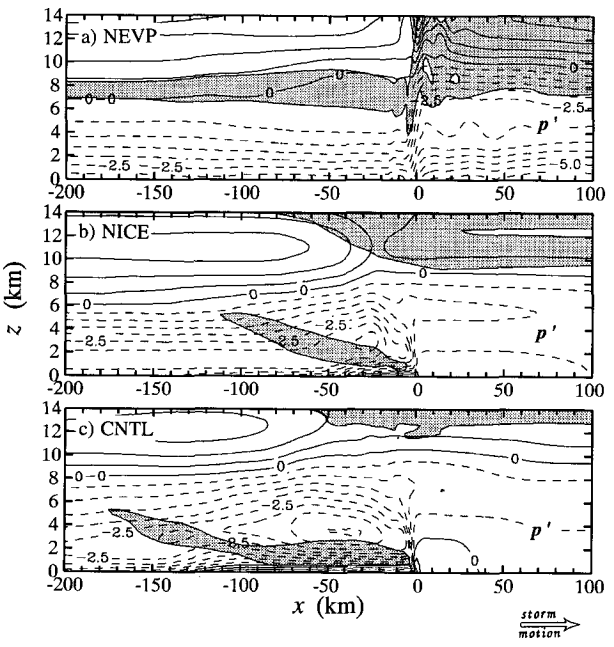

FIG. 19. One-hour-averaged ($t = 10$–11 h) pressure perturbation p' (contour interval is 0.5 mb) of (a) the NEVP run, (b) the NICE run, and (c) the CNTL run. Positive field is in solid lines; negative field is dashed. Rear-to-front flow greater than 5 m s^{-1} is shaded.

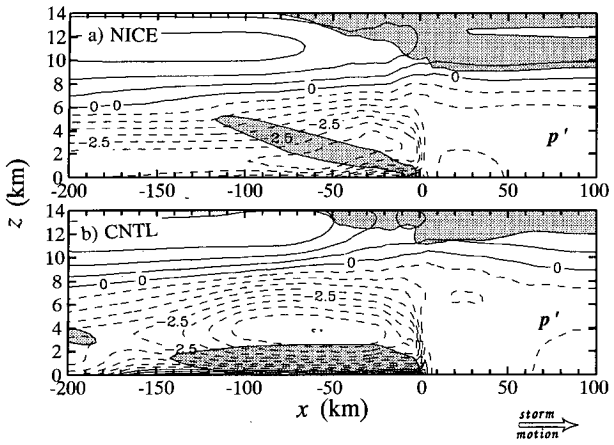

FIG. 20. One-hour-averaged (t = 12.5–13.5 h) pressure perturbation p' (contour interval is 0.5 mb) of (a) the NICE run and (b) the CNTL run. Positive field is in solid lines; negative field is dashed. Rear-to-front flow greater than 5 m s^{-1} is shaded.

trailing stratiform regions are absent, there is *no* descending rear inflow; the rear inflow remains elevated. The rear inflow results from environmental winds entering and overtaking the storm. When the stratiform region is narrow and weak, as in the no-ice run (NICE; Fig. 19b), there is only one mesolow that is due to the slope of the convective cells in the leading line (LeMone 1983). In this case, there is only *one* RTF wind maximum. In the full-physics control run (CNTL; Fig. 19c), the low at the back of the convective cells is broader, and a second mesolow is at the back edge of the stratiform region. The mesolow in the stratiform region is *collocated* with the RTF wind maximum at the back edge of the stratiform precipitation ($x = -160$ to -130 km). This structure is consistent with Smull and Houze's suggestion that the resulting horizontal-pressure-gradient force associated with the stratiform region mesolow draws midlevel air into the storm from the rear to induce the rear inflow.

The RTF flow during the late stage of the NICE storm (Fig. 20a) has the same width, intensity, and slope as in the mature stage (Fig. 19b). However, in the late stage of the full-physics CNTL run (Fig. 20b), the mesolow in the convective region is broader and stronger, and the two RTF maxima are more distinct and more widely separated from each other than in the mature stage (Fig. 19c). With ice-phase microphysics included, the RTF flow (Fig. 20b) descends and spreads along the surface well behind the leading edge of the storm. The enhanced RTF flow at the back edge of the storm ($x = -200$ km) is located farther rearward in the late stage, consistent with radar observations (see Figs. 5–7 of Rutledge et al. 1988).

Since large-scale baroclinic processes are inoperative and the descending rear inflow in this model is caused entirely by the storm-induced circulation, this study confirms the conclusion of Smull and Houze (1987) and Lafore and Moncrieff (1989) that the rear inflow can be generated by physical processes internal to the MCS. The good correspondence of the midlevel mesolow in the convective (stratiform) region to the maximum RTF flow at the rear of the convective (stratiform) region (in the CNTL run) further supports Smull and Houze's argument that two separate midlevel mesolows are involved in the development of the RTF flow and that the two mesolows may act constructively to establish a continuous RTF flow channel across the storm.

6. Conclusions

Two-dimensional simulations of the 10–11 June 1985 squall line in PRE-STORM with a high-resolution nonhydrostatic convection-resolving model reproduce a storm structure that agrees with the detailed observations obtained in this case. Despite two-dimensional geometry and neglect of the Coriolis force, large-scale motion, radiation, and surface drag, the microphysical, kinematic, thermal, and pressure structures are well simulated.

The ascending FTR flow transports hydrometeors across the system from the leading-edge convective line to the trailing stratiform region. The FTR flow becomes stronger and more horizontally tilted with time. The descending RTF flow enters the storm from the rear and penetrates into the convective region at low levels. As the system matures and expands, the RTF flow shows a double-core structure. A maximum of RTF flow located at the back edge of the stratiform precipitation consists of midlevel environmental air from the rear of the storm.

The mesoscale updraft and downdraft become organized once the system is well developed and they reach their maximum strength during the mature stage. Air parcel trajectory analysis indicates that most of the air within mesoscale updrafts originally comes from the high-θ_e boundary layer ahead of the system. About half of the air within mesoscale downdraft is from the leading-edge convective region, and the other half is from the poststorm midlevel low-θ_e layers. Precipitation particles falling into the transition zone are from the low levels of the convective region, and those falling into the stratiform region are from the mid- to upper-levels of the convective region, consistent with the results of Biggerstaff and Houze (1993) and Braun and Houze (1994).

Most of the latent heating in the cloudy region is produced by condensational warming of cloud water, and most of the latent cooling in the subcloud region is produced by evaporative cooling of rainwater. Depositional growth of ice particles in the stratiform cloud region adds additional latent heating and enhances the mesoscale updraft. The structure and strength of the rear inflow is found to be sensitive to precipitating hydrometeor types, ice-phase microphysics, and the latent

cooling of evaporation, melting, and sublimation. A series of sensitivity tests isolates and quantifies the role of each of these microphysical processes in the generation and maintenance of the descending RTF flow. Table 2 summarizes the main results of each test.

In the HAIL test, hailstones are allowed to form throughout the mature and decaying stages. Hail particles fall out so quickly that the surface precipitation region is much narrower than in the control case (CNTL), in which there are no hailstones after the initial stage. The stratiform precipitation region is weak and narrow. The broad and uniform mesoscale updraft/downdraft does not occur. There is only one maximum of RTF flow within the storm; no second maximum occurs at the back edge, because the midlevel mesolow in the stratiform region is too weak. The realistic structure of the simulated descending rear inflow (at least for the 10–11 June 1985 squall line) thus appears to be sensitive to the hydrometeor types, which affect the kinematic structure of the storm through their fallout pattern and the subsequent effects of diabatic processes on the thermal and pressure fields.

Stratiform precipitation and the enhanced RTF flow at the back edge of the storm in the no-ice run (NICE) are not as realistic as in the CNTL run. The lack of ice microphysics and realistic stratiform precipitation implies that none of the key cooling processes in the production of the rear inflow—sublimation, melting, and evaporation—can occur in the stratiform region. The NICE test thus shows that ice microphysics are crucial to the proper existence of the descending rear inflow and mesoscale updraft/downdraft.

In the test with evaporative cooling turned off (NEVP), the system is upright to downshear-tilted, with stratiform precipitation ahead of the convective region. There is no mesoscale ascent or descent. There is no mid-to-upper-level FTR flow transporting hydrometeors rearward. The RTF flow is elevated, a consequence of strong midlevel winds in the environment overtaking and entering the storm. The NEVP test thus supports the argument of Smull and Houze (1987) that the descending rear inflow and mesoscale downdraft develop in response to the dynamical and microphysical feedbacks (in particular, the evaporative cooling) of the storm.

The no-melting-cooling (NMLT) storm is more upright compared to the CNTL case. The double maximum structure of the RTF flow is well preserved, indicating that the cooling by melting is not the cause of rear inflow. However, this experiment shows that the latent cooling by melting accounts for at least 25% of the intensity of the peak RTF flow at the back edge of the storm during the mature stage, confirming the impact of melting cooling on the stratiform region RTF flow suggested by Smull and Houze (1987) and Rutledge et al. (1988). The mesoscale ascent of the NMLT storm is somewhat stronger, and the mesoscale descent is 22% weaker and 33% narrower. Therefore, cooling by melting does not initiate the mesoscale downdraft (as suggested by Leary and Houze 1979), but does strongly enhance the mesoscale downdraft.

The test NSUB (latent cooling by sublimation turned off) shows that sublimational cooling only slightly affects the strength of the rear inflow. However, sublimation at the base of the anvil cloud at the rear of the trailing stratiform region is key to the initiation of downward air motion above the 0°C level (z = 4 km) at the rear of the storm, as suggested by Rutledge et al. (1988).

The test DRYM shows that with only half of the initial midlevel moisture the mesoscale downdraft is 22% stronger, but the maximum of RTF flow at the rear of the system is 62% weaker. The weaker stratiform region RTF flow is due to the weaker horizontal buoyancy gradients at the back edge of the storm, which result from a more upright system orientation. When drier environmental air is entrained into the storm, it enhances the evaporative cooling at midlevels at the leading edge and counteracts the upshear tilt induced by the cold-pool circulation.

In summary, the descending rear inflow is partly a dynamical response to the latent cooling processes in squall-line trailing stratiform precipitation. The role of mesolows in the formation of the descending RTF flow is discussed, and the numerical experiments confirm the argument of Smull and Houze (1987): the stratiform

TABLE 2. Summary of mature-stage RTF flow structure of experimental simulations.

Run	Storm speed	Storm orientation	RTF flow structure
CNTL	12.2 m s^{-1}	upshear tilt	two maximum in the storm (8 m s^{-1})*
HAIL	11 m s^{-1}	upshear tilt	one maximum in convective region
NICE	8 m s^{-1}	upshear tilt	one maximum in convective region
NEVP	5 m s^{-1}	upright to downshear tilt	a highly elevated RTF flow
NMLT	12 m s^{-1}	less upshear tilt	two maximum in the storm (6 m s^{-1})
NSUB	10.8 m s^{-1}	less upshear tilt	two maximum in the storm (7 m s^{-1})
DRYM	12.2 m s^{-1}	more upright	two maximum in the storm (3 m s^{-1})

* Number in the parentheses is the maximum of RTF flow at the back edge of the stratiform precipitation during the mature stage (t = 10–11 h).

region mesolow acts constructively with the convective region mesolow to establish a continuous RTF flow across the system. Evaporative cooling is the most important latent cooling process determining the descending RTF flow. The descent of the rear inflow and the mesoscale downdraft are initiated above the 0°C level by sublimation at the base of the trailing cloud anvil. Melting does not initiate the mesoscale downdraft but strongly enhances both the mesoscale downdraft and the RTF flow in the stratiform region. Evaporation accounts for most of the structure and strength of the descending RTF flow, but without ice-phase microphysics, neither the realistic stratiform precipitation nor the enhanced RTF flow at the back edge of the storm can occur. Finally, correct types of ice particles must be included in the model in order to have a proper structure of the descending RTF flow, at least for the 10–11 June 1985 squall line.

An important implication of this study is that parameterization of MCSs in a large-scale general circulation model (GCM) is not simple. A slight change of hydrometeor types, ice microphysics, and environmental humidity can significantly affect the storm structure and hence momentum and moisture transports, radiation budget, and the interaction with the surrounding large-scale environment. Therefore, the proper handling of microphysical processes is necessary in order to have a reasonable representation of the effects of MCSs in a GCM.

Acknowledgments. Professor R. G. Fovell guided the early modeling of the storm. S. A. Braun, H.-N. S. Chin, D. R. Durran, R. Pandya, B. F. Smull, M. L. Weisman, D.-L. Zhang, and anonymous reviewers provided helpful comments and improved the paper substantially. G. C. Gudmundson edited the manuscript and Kay Dewar drafted some of the figures. The simulations were performed at the National Center for Supercomputing Applications (NCSA) at the University of Illinois at Urbana–Champaign. This research was supported by NSF Grants ATM-9101653 and ATM-9409988.

REFERENCES

Augustine, J. A., and E. J. Zipser, 1987: The use of wind profilers in a mesoscale experiment. *Bull. Amer. Meteor. Soc.*, **68,** 4–17.

Biggerstaff, M. I., and R. A. Houze Jr., 1991a: Kinematic and precipitation structure of the 10–11 June 1985 squall line. *Mon. Wea. Rev.*, **119,** 3034–3065.

——, and ——, 1991b: Midlevel vorticity structure of the 10–11 June 1985 squall line. *Mon. Wea. Rev.*, **119,** 3066–3079.

——, and ——, 1993: Kinematics and microphysics of the transition zone of the 10–11 June 1985 squall line. *J. Atmos. Sci.*, **50,** 3091–3110.

Bluestein, H. B., and M. H. Jain, 1985: Formation of mesoscale lines of precipitation: Severe squall lines in Oklahoma during spring. *J. Atmos. Sci.*, **42,** 1711–1732.

Braun, S. A., 1995: Multiscale process interactions associated with a midlatitude squall line. Ph.D. dissertation, University of Washington, 194 pp.

——, and R. A. Houze Jr., 1994: The transition zone and secondary maximum of radar reflectivity behind a midlatitude squall line: Results retrieved from Doppler radar data. *J. Atmos. Sci.*, **51,** 2733–2755.

Brown, J. M., 1979: Mesoscale unsaturated downdrafts driven by rainfall evaporation: A numerical study. *J. Atmos. Sci.*, **36,** 313–338.

Chin, H.-N. S., 1994: The impact of the ice phase and radiation on a midlatitude squall line system. *J. Atmos. Sci.*, **51,** 3320–3343.

Chong, M., P. Amayenc, G. Scialom, and J. Testud, 1987: A tropical squall line observed during the COPT 81 experiment in West Africa. Part I: Kinematic structure inferred from dual-Doppler radar data. *Mon. Wea. Rev.*, **115,** 670–694.

Churchill, D. D., and R. A. Houze Jr., 1984: Development and structure of winter monsoon cloud clusters on 10 December 1978. *J. Atmos. Sci.*, **41,** 933–960.

Cunning, J. B., 1986: The Oklahoma–Kansas Preliminary Regional Experiment for STORM-Central. *Bull. Amer. Meteor. Soc.*, **67,** 1478–1486.

Doty, K. G., and D. J. Perkey, 1993: Sensitivity of trajectory calculations to the temporal frequency of wind data. *Mon. Wea. Rev.*, **121,** 387–401.

Dudhia, J. M., W. M. Moncrieff, and D. W. K. So, 1987: The two-dimensional dynamics of West African squall lines. *Quart. J. Roy. Meteor. Soc.*, **113,** 121–146.

Fovell, R. G., and Y. Ogura, 1988: Numerical simulation of a midlatitude squall line in two dimensions. *J. Atmos. Sci.*, **45,** 3846–3879.

——, and ——, 1989: Effects of vertical wind shears on numerically simulated multicell storm structure. *J. Atmos. Sci.*, **46,** 3144–3176.

Fritsch, J. M., and C. F. Chappell, 1980: Numerical prediction of a convectively driven mesoscale pressure system. Part I: Convective parameterization. *J. Atmos. Sci.*, **37,** 1722–1733.

Fujita, T. T., 1955: Results of detailed synoptic studies of squall lines. *Tellus*, **7,** 405–436.

Hamilton, R. A., and J. W. Archbold, 1945: Meteorology of Nigeria and adjacent territory. *Quart. J. Roy. Meteor. Soc.*, **71,** 303–314.

Houze, R. A., Jr., 1977: Structure and dynamics of a tropical squall line system. *Mon. Wea. Rev.*, **105,** 1540–1567.

——, 1993: *Cloud Dynamics.* Academic Press, 573 pp.

——, B. F. Smull, and P. Dodge, 1990: Mesoscale organization of springtime rainstorms in Oklahoma. *Mon. Wea. Rev.*, **118,** 613–654.

——, S. A. Rutledge, M. I. Biggerstaff, and B. F. Smull, 1989: Interpretation of Doppler weather radar displays of midlatitude mesoscale convective systems. *Bull. Amer. Meteor. Soc.*, **70,** 608–619.

Johnson, R. H., and P. J. Hamilton, 1988: The relationship of surface pressure features to the precipitation and the airflow structure of an intense midlatitude squall line. *Mon. Wea. Rev.*, **116,** 1444–1472.

Klemp, J. B., and R. B. Wilhelmson, 1978: The simulation of three-dimensional convective storm dynamics. *J. Atmos. Sci.*, **35,** 1070–1096.

Lafore, J.-P., and M. W. Moncrieff, 1989: A numerical investigation of the organization and interaction of the convective and stratiform regions of tropical squall lines. *J. Atmos. Sci.*, **46,** 521–544.

Leary, C. A., and R. A. Houze Jr., 1979: Melting and evaporation of hydrometeors in precipitation from anvil clouds of deep tropical convection. *J. Atmos. Sci.*, **36,** 669–679.

LeMone, M. A., 1983: Momentum flux by a line of cumulonimbus. *J. Atmos. Sci.*, **40,** 1815–1834.

Lin, Y. L., R. D. Farley, and H. D. Orville, 1983: Bulk parameterization of the snow field in a cloud model. *J. Climate Appl. Meteor.*, **22,** 1066–1092.

Mapes, B. E., 1993: Gregarious tropical convection. *J. Atmos. Sci.*, **50,** 2026–2037.

Moncrieff, M. W., and M. J. Miller, 1976: The dynamics and simulation of tropical cumulonimbus and squall lines. *Quart. J. Roy. Meteor. Soc.*, **102,** 373–394.

Newton, C. W., 1950: Structure and mechanism of a prefrontal squall line. *J. Meteor.*, **7,** 210–222.

Nicholls, M. E., 1987: A comparison of the results of a two-dimensional numerical simulation of a tropical squall line with observations. *Mon. Wea. Rev.*, **115,** 3055–3077.

Orlanski, I., 1975: A rational subdivision of scales for atmospheric processes. *Bull. Amer. Meteor. Soc.*, **56,** 527–530.

Pedgley, D. E., 1962: A meso-synoptic analysis of the thunderstorms on 28 August 1958. British Meteorological Office, Geophys. Memo., 106, 74 pp.

Potter, B. E., 1991: Improvement to a commonly used cloud microphysical bulk parameterization. *J. Appl. Meteor.*, **30,** 1040–1042.

Redelsperger, J.-L., and J.-P. Lafore, 1988: A three-dimensional simulation of a tropical squall line: Convective organization and thermodynamical vertical transport. *J. Atmos. Sci.*, **45,** 1334–1356.

Rotunno, R., J. B. Klemp, and M. L. Weisman, 1988: A theory for strong, long-lived squall lines. *J. Atmos. Sci.*, **45,** 463–485.

Roux, F., J. Testud, M. Payen, and B. Pinty, 1984: West African squall line thermodynamic structure retrieved from dual-Doppler radar observations. *J. Atmos. Sci.*, **41,** 3104–3121.

Rutledge, S. A., and R. A. Houze Jr., M. I. Biggerstaff, and T. Matejka, 1988: The Oklahoma–Kansas mesoscale convective system of 10–11 June 1985: Precipitation structure and single-Doppler radar analysis. *Mon. Wea. Rev.*, **116,** 1409–1430.

Skamarock, W. C., M. L. Weisman, and J. B. Klemp, 1994: Three-dimensional evolution of simulated long-lived squall lines. *J. Atmos. Sci.*, **51,** 2563–2584.

Smull, B. F., and R. A. Houze Jr., 1985: A midlatitude squall line with a trailing region of stratiform rain: Radar and satellite observations. *Mon. Wea. Rev.*, **113,** 117–133.

——, and ——, 1987: Rear inflow in squall lines with trailing stratiform precipitation. *Mon. Wea. Rev.*, **115,** 2869–2889.

Szeto, K. K., and H.-R. Cho, 1994: A numerical investigation of squall lines. Part II: The mechanics of evolution. *J. Atmos. Sci.*, **51,** 425–433.

Tao, W.-K., and J. Simpson, 1989: Modeling study of a tropical squall-type convective line. *J. Atmos. Sci.*, **46,** 177–202.

——, ——, and S.-T. Soong, 1991: A numerical study of a squall line over the Taiwan Strait during TAMEX IOP 2. *Mon. Wea. Rev.*, **119,** 2699–2723.

——, J. R. Scala, C.-H. Sui, B. Ferrier, S. Lang, J. Scala, M. D. Chou, and K. Pickering, 1993: Heating, moisture, and water budgets of tropical and midlatitude squall lines: Comparisons and sensitivity to longwave radiation. *J. Atmos. Sci.*, **50,** 673–690.

——, ——, B. Ferrier, and J. Simpson, 1995: The effects of melting processes on the development of squall lines in the Tropics and midlatitudes. *J. Atmos. Sci.*, **52,** 1934–1948.

Weisman, M. L., 1992: The role of convectively generated rear-inflow jets in the evolution of long-lived mesoconvective systems. *J. Atmos. Sci.*, **49,** 1826–1847.

——, and J. B. Klemp, 1982: The dependence of numerically simulated convective storms on wind shear and buoyancy. *Mon. Wea. Rev.*, **110,** 504–520.

——, ——, and R. Rotunno, 1988: Structure and evolution of numerically simulated squall lines. *J. Atmos. Sci.*, **45,** 1990–2013.

Wilhelmson, R. B., and C.-S. Chen, 1982: A simulation of the development of successive cells along a cold outflow boundary. *J. Atmos. Sci.*, **39,** 1466–1483.

Yang, M.-J., and R. A. Houze Jr., 1995: Multicell squall-line structure as a manifestation of vertically trapped gravity waves. *Mon. Wea. Rev.*, **123,** 641–661.

Zhang, D.-L., and K. Gao, 1989: Numerical simulation of an intense squall line during 10–11 June 1985 PRE-STORM. Part II: Rear inflow, surface wake lows and stratiform precipitation. *Mon. Wea. Rev.*, **117,** 2067–2094.

——, ——, and D. B. Parsons, 1989: Numerical simulation of an intense squall line during 10–11 June 1985 PRE-STORM. Part I: Model verification. *Mon. Wea. Rev.*, **117,** 960–994.

Zipser, E. J., 1969: The role of organized unsaturated convective downdrafts in the structure and rapid decay of an equatorial disturbance. *J. Appl. Meteor.*, **8,** 799–814.

——, 1977: Mesoscale and convective-scale downdrafts as distinct components of squall-line circulation. *Mon. Wea. Rev.*, **105,** 1568–1589.